

Cite this: *Catal. Sci. Technol.*, 2018, 8, 5244

Cobalt nanoparticles incorporated into hollow doped porous carbon capsules as a highly efficient oxygen reduction electrocatalyst†

Feng Guo,^{*ab} Hui Yang,^{*b} Briana Aguila,^{id b} Abdullah M. Al-Enizi,^c Ayman Nafady,^{cd} Mandeep Singh,^e Vipul Bansal^{id e} and Shengqian Ma^{id *bc}

Platinum-based materials have been the dominant and best electrocatalysts for promoting the oxygen reduction reaction (ORR). However, going beyond state-of-the-art catalysts remains a great challenge. Recently, nanostructured composites of conductive carbons and earth-abundant metals have emerged as promising electrocatalysts. Herein, we report a facile and practical approach for the synthesis of cobalt nanoparticles embedded into hollow nitrogen/cobalt-doped porous carbon capsules (Co@NPCC). The fabrication of this material was achieved *via* the thermal decomposition of sacrificial metal-organic framework nanocrystals coated with a metal-tannic acid coordination polymer shell, upon pyrolysis, which delivers zerovalent cobalt nanoparticles embedded in the walls of hollow capsules. Co@NPCC proved to be a superb catalyst for the electrochemical ORR, showing a highly positive onset potential (~ 1.02 V vs. RHE) and current density (~ 5.2 mA cm⁻²) in 0.1 M KOH electrolyte. These values are in excellent agreement with those reported for the state-of-the-art Pt/C catalyst. Significantly, materials produced *via* this approach can be manufactured on a large scale, thereby providing access to next-generation catalysts for important electrochemical processes.

Received 2nd July 2018,
Accepted 10th September 2018

DOI: 10.1039/c8cy01371c

rsc.li/catalysis

Introduction

The electrochemical oxygen reduction reaction (ORR) is the heart of fuel cells and lithium-air batteries. In general, platinum-based materials are the most active and stable catalysts for the ORR.^{1–3} However, the scarcity and high cost of platinum limits their practical utility in large-scale applications. To overcome these drawbacks while maintaining or improving the catalytic activity, exploring cheap, efficient, and durable alternatives to platinum is crucial to facilitate the global scalability of such potential clean energy technology.^{4–9}

Recently, as newly developed catalysts, metal species supported nitrogen-doped carbon materials have emerged as one of the most promising alternatives to ORR catalysts.^{10–19} Since the attractive functional properties of these catalysts

primarily rest in their chemical components and porous geometries, small and monodisperse metal nanoparticles (NPs) are highly desirable.^{10,12,15,20} However, it remains a challenge to prepare such materials while avoiding the sintering or aggregation of the NPs. Support materials, particularly those based on carbon, have been used to address this issue. A highly desirable feature in these carbon supports is their discrete and hollow character, which gives rise to the formation of hollow porous carbon capsules (PCCs). The attractive structural features of hollow porous carbon capsules include uniform size/shape, large surface area, large interior void spaces, and highly porous walls, which expose the active sites of the catalyst to the reaction environment and help accelerate mass transfer processes during chemical reactions. Furthermore, heteroatom doping (*e.g.*, B, S, N, P, *etc.*) within these porous materials has been demonstrated as an effective strategy to improve their activity in the aforementioned applications.^{21–29} To achieve this substitution, a few metal-organic framework (MOF)-derived porous carbon support non-precious metal catalysts^{20,29–53} have been synthesized. However, it is still a prime challenge to achieve large-scale preparation of non-precious nanoparticles embedded in heteroatom-doped hollow carbon capsules at the cutting edge of this field of research.

In this work, we report a generic approach for the large-scale synthesis of cobalt nanoparticles embedded in hollow

^a Chongqing Key Laboratory of Inorganic Special Functional Materials, College of Chemistry and Chemical Engineering, Yangtze Normal University, 16 Juxian Rd, Fuling, Chongqing, 408100 China. E-mail: guofeng1510@yeah.net

^b Department of Chemistry, University of South Florida, CHE205A, 4202E. Fowler Avenue, Tampa, Florida, 33620, USA. E-mail: huiy@mail.usf.edu, sqma@usf.edu

^c Chemistry Department, College of Science, King Saud University, Riyadh, 11451, Saudi Arabia

^d Chemistry Department, Faculty of Science, Sohag, 82524, Egypt

^e Ian Potter NanoBioSensing Facility, NanoBiotechnology Research Laboratory, School of Science, RMIT University, Melbourne, VIC, 3000, Australia

† Electronic supplementary information (ESI) available. See DOI: 10.1039/c8cy01371c

cobalt–nitrogen-doped porous carbon capsules (Co@NPCC). Our methodology for achieving this is summarized in Scheme 1. MOF nanocrystals are employed to define the shape and size for the hollow structure. Here, the MOF is ZIF-8CoZn. A uniform layer of a potassium–tannic acid polymer is then deposited around the ZIF nanocrystals from soluble precursors (step I). This produces a ZIF-8CoZn@K-TA composite material. Pyrolysis of this composite yields hollow cobalt–nitrogen-doped carbon capsules that support cobalt nanoparticles (Co@NPCC) (step II). This material presents many attractive structural features for electrocatalysis, including uniformly dispersed cobalt nanoparticles in graphitic layers, exposed Co–N_x active sites, and excellent permeability to incoming gases. Benefitting from the structure, Co@NPCC demonstrates outstanding oxygen reduction reaction (ORR) performance with low onset potential, high current density, four-electron transfer, and long-term durability in alkaline media. Our results provide a useful platform for the design and fabrication of economical and efficient large-scale electrocatalysts.

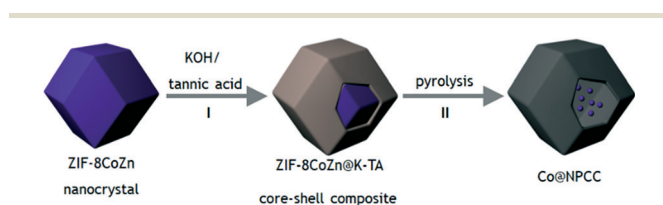
Experimental section

Materials

All starting compounds and solvents were used as obtained from commercial sources without further purification unless otherwise noted.

Synthesis of ZIF-8CoZn. ZIF-8CoZn nanocrystals were prepared using a reported procedure with a slight modification.³⁹ In a typical synthesis, 4 g of 2-methylimidazole was dissolved in 60 mL of MeOH to form a clear solution. 1.65 g of Zn(NO₃)₂·6H₂O and 0.03 g of Co(NO₃)₂·6H₂O in 20 mL MeOH were added into the above solution with vigorous stirring for 1 h. The mixture was then incubated at room temperature without stirring. After 24 h, the product was isolated as a light purple powder by centrifugation and washed several times with MeOH, and finally dried overnight under vacuum.

Synthesis of ZIF-8CoZn@K-TA. In a typical synthesis, 10 g of ZIF-8CoZn nanocrystals were dispersed in 200 mL of deionized water. Separately, a freshly prepared tannic acid solution (24 mM, 100 mL) was adjusted to pH 8 by the addition of aqueous KOH solution (6 M). Subsequently, the suspension of ZIF-8CoZn nanocrystals was added to the tannic acid solution. After stirring for 10 min, ZIF-8CoZn@K-TA was collected by centrifugation, washed several times with deionized water and methanol, and dried overnight under vacuum.



Scheme 1 Schematic illustration showing the synthetic route to cobalt nanoparticles embedded in hollow doped porous carbon capsules.

Large-scale synthesis of Co@NPCC

10 g of ZIF-8CoZn@K-TA was placed in a furnace under a dry nitrogen flow and heated from room temperature to 900 °C over a period of 100 min. After reaching the target temperature, the sample was calcined for a further 3 h at 900 °C then cooled to room temperature to give Co@NPCC (NPCC = hollow nitrogen-doped porous carbon capsule), which was washed with 0.2 M HNO₃, deionized water and methanol, then dried overnight under vacuum. Yield: 3.63 g of Co@NPCC.

Instrumentation

Powder X-ray diffraction (PXRD) was performed on a Rigaku X-ray diffractometer with a Cu K α source. BET surface areas were determined from N₂ adsorption/desorption isotherms at 77 K using automatic volumetric adsorption equipment (ASAP 2020) after pre-treatment under vacuum at 100 °C for 12 h. Scanning electron microscopy (SEM) images and energy dispersive spectra (EDS) were recorded on a FEI Quanta 200 environmental scanning electron microscope. Transmission electron microscope (TEM) images were recorded on an FEI Tecnai G² BioTwin transmission electron microscope operating at an accelerating voltage of 100 kV. High resolution transmission electron microscopic (HRTEM) analysis was carried out with a TECNAI F20 transmission electron microscope operating at an accelerating voltage of 200 kV. STEM images, EDS mapping and electron energy loss spectroscopy (EELS) profile were obtained on a JEOL 2100F microscope operating at 200 kV accelerating voltage. EELS was performed in STEM mode. Multiple EELS spectra were recorded as a line profile along the particle surface to validate the absence of oxygen in cobalt particles. Inductively coupled plasma atomic emission spectroscopy (ICP-AES) was conducted on a Jobin Yvon Horiba–Ultima 2 spectrometer system. Elemental analyses (EA) were performed on a Vario MICRO analysis system. Raman spectra were measured from powder samples with a Cobalt Samba single-mode 532 nm diode laser on quartz substrates. X-ray photoelectron spectroscopy (XPS) analyses of Co@NPCC were performed using a Kratos Axis DLD spectrometer. And the XPS measurements of ZIF-8@CoZn-TA were performed on a K-alpha spectrometer (Thermo Scientific) using a monochromatic Al-K α (1486.7 eV) radiation source at room temperature under ultra-high vacuum (10^{−8} Pa). Fourier transform infrared spectra (FTIR) were recorded on a ThermoElectron Nicolet high-resolution FT-MIR/FT-FarIR. The ORR tests were performed with a pine electrochemical analyser (AFMSRCE Electrode Rotator WaveDriver 20 Bipotentiostat/Galvanostat System, USA).

Electrochemical measurements

The ORR tests were performed with a Pine electrochemical analyser (AFMSRCE Electrode Rotator WaveDriver 20 Bipotentiostat/Galvanostat System, USA) in an aqueous 0.1 M KOH or 0.05 M H₂SO₄ electrolyte at room temperature. All

electrochemical measurements were conducted in a standard three-electrode system completed with a platinum counter electrode and an Ag/AgCl (3.5 M KCl) reference electrode. A glassy carbon (GC) rotating disk electrode (RDE, 5.0 mm in diameter, 0.196 cm², Pine, USA) or a rotating ring disk electrode (RRDE) supported the as-synthesized materials on the working electrode with the rotation rate varying from 300 to 2200 rpm. 5 mg of Co@NPCC, Co/NC, or Pt/C (20 wt% of Pt) was dispersed in 1.1 mL of ethanol and 100 μ L of deionized water (containing 100 μ L of 5.0 wt% Nafion) solution under ultrasonic agitation to form an electrocatalyst ink. The ink was dropped on the surface of the pre-cleaned rotating disk working electrode and dried at room temperature. The catalyst loading was determined to be 0.1 mg cm⁻². CVs were recorded in nitrogen (or oxygen) saturated aqueous (0.1 M KOH or 0.05 M H₂SO₄) electrolytes using a scan rate of 20 mV s⁻¹. The LSV curves were recorded at a scan rate of 5 mV s⁻¹. Commercial Pt/C (20 wt% of Pt) was employed for comparison. Long-term stability tests for the Co@NPCC catalyst were accomplished by conducting 10000 CV cycles in 0.1 M KOH (5000 cycles in 0.05 M H₂SO₄) at a scan rate of 50 mV s⁻¹.

Results and discussion

Synthesis and characterization of the Co@NPCC catalyst

ZIF-8CoZn nanocrystals were first prepared *via* a facile synthetic route in aqueous solution at room temperature.³⁹ The morphologies of the ZIF-8CoZn nanocrystals were examined by scanning electron microscopy (SEM) and transmission electron microscopy (TEM), and found to be dodecahedral with edge lengths of 50 to 350 nm (Fig. S1 and S2[†]). When coated with a coordination polymer comprising potassium-tannic acid (K-TA), a ZIF-8CoZn@K-TA core-shell composite was obtained (Fig. S1, S3, S4 and S5[†]).⁵⁴ Here, abundant hydroxyl and galloyl groups of TA have strong chelating ability with potassium cations and zinc/cobalt(II) metal cations on the surface of ZIF-8CoZn. The FTIR spectrum of ZIF-8CoZn@K-TA exhibits peaks attributable to both the TA and ZIF-8CoZn components (Fig. S4[†]). This is further confirmed by X-ray photoelectron spectroscopy (XPS) (Fig. S5[†]). The organic components of the composite form a hollow capsule upon pyrolysis (Fig. 1 and S7[†]). The tannic acid coordination polymer shell plays a crucial role in directing the formation of the hollow capsules; dense particles form in its absence (Fig. S6[†]).

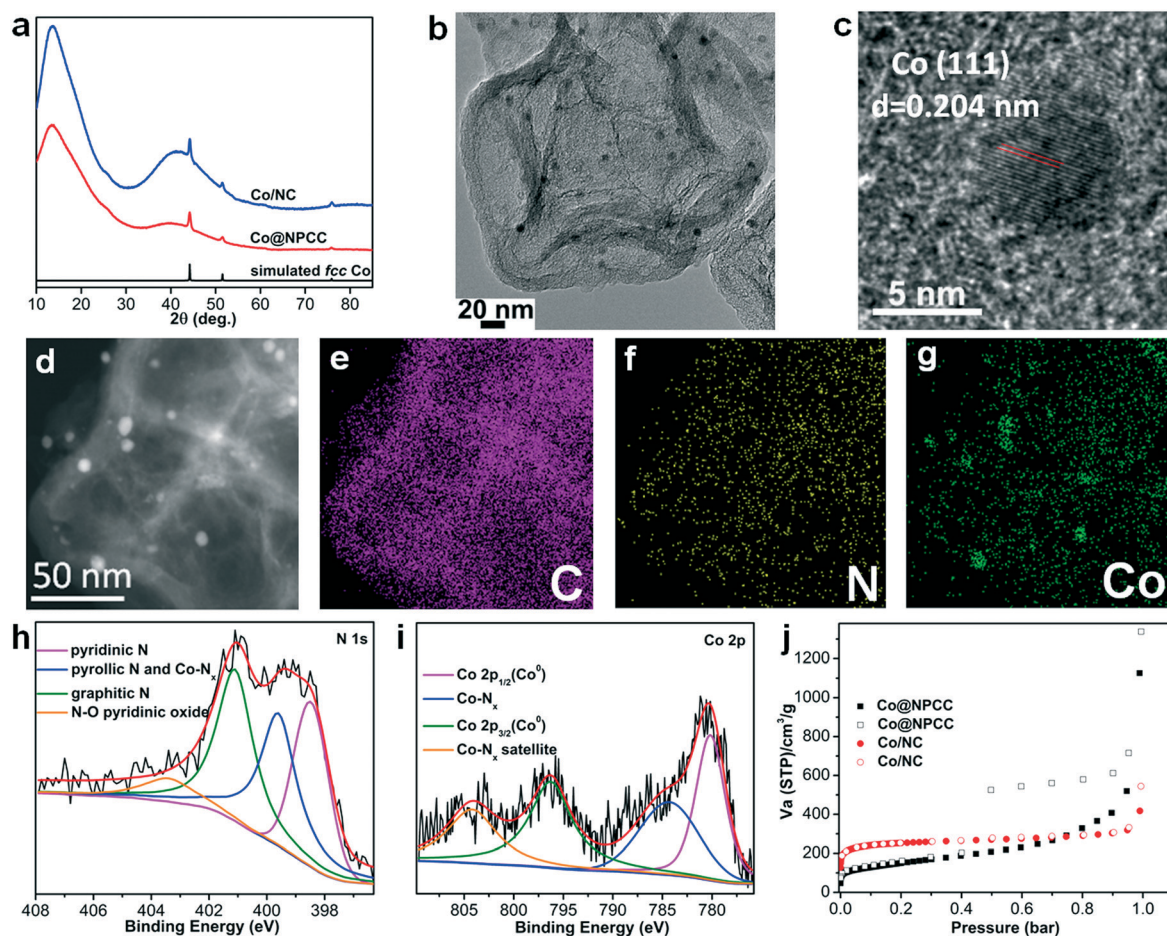


Fig. 1 (a) PXRD pattern of materials. (b) TEM image of Co@NPCC. (c) HRTEM image of an individual CoNP. (d–g) STEM image and elemental mapping of Co@NPCC. XPS spectra of (h) N 1s and (i) Co 2p of Co@NPCC. (j) N₂ adsorption (filled symbols) and desorption (open symbols) isotherms measured at 77 K.

The cobalt ions are reduced to cobalt metal during the pyrolysis step. The PXRD pattern of the Co@NPCC composite (Fig. 1a) correlates with that of *fcc* Co (Powder Diffraction File no. 89-4307, Joint Committee on Powder Diffraction Standards, 2013). No diffraction peaks from CoO or Co₃O₄ were detected, which indicates that the cobalt exists exclusively in its zerovalent state. The SEM image reveals the dodecahedral capsule morphology observed for Co@NPCC (Fig. S7a†). TEM images confirm the hollow nature of the Co@NPCC hosts and the localization of the CoNPs on the capsule walls (Fig. 1b and S7b†). No sintering of the nanoparticles into large aggregates was evident, and no nanoparticles were observed on the exterior of the carbon shell. The average diameter of the CoNPs in Co@NPCC is ~4.3 nm (Fig. S8†). HRTEM images of individual CoNPs clearly reveal lattice fringes with an interplanar spacing of 2.04 Å, corresponding to contrast profiles of the cubic Co (111) planes (Fig. 1c). The peaks in the selected area electron diffraction (SAED) pattern of Co@NPCC can be indexed to the (111), (200), (220), and (311) planes of the Co nanoparticles (Fig. S9†). STEM imaging and EDS mapping confirm that the Co, C, and N components are uniformly distributed (Fig. 1d–g). Electron energy loss spectroscopy (EELS) and line scan analysis exhibited a uniform distribution of the metallic cobalt. No oxygen element was observed (Fig. S10†).

X-ray photoelectron spectroscopy (XPS) was applied to elucidate the details of the chemical composition and the electronic states of C, N and Co in Co@NPCC. The XPS spectra of Co@NPCC demonstrate the presence of cobalt, carbon, and nitrogen (Fig. 1h, i and S11†). The high-resolution C 1s XPS spectrum of Co@NPCC presents five characteristic peaks, where the peak at 284.6 eV corresponds to the sp²/sp³ hybridized graphitic carbon, the peak around 283.7 eV is consistent with cobalt carbide, and the peaks at 285.9 and 288.1 eV are assigned to carbon in C–N and C=O bonds, respectively (Fig. S11†). The N 1s high-resolution spectrum suggests the existence of N dopants in the carbon of the capsules, with three peaks corresponding to pyridine-like N (398.1 eV), pyrrole-like N (399.8 eV), graphitic N (401.5 eV), and N–O pyridine-like (403.7 eV) moieties (Fig. 1h). All of these dopant sites promote the ORR catalytic performance, which is of relevance to electrocatalytic oxygen reduction tests discussed below. Co 2p_{1/2} and Co 2p_{3/2} bands were observed at 779.2 and 795.1 eV, respectively, which are in agreement with values reported for zero-valent cobalt (Fig. 1i).^{39,46} Furthermore, two shoulder peaks were observed at 784.3 and 803.2 eV corresponding to Co–N_x and satellites, respectively.^{39,46} It has been previously confirmed that both Co–N_x active sites and Co nanoparticles have been previously proved to merit the ORR.^{39,46,55} The Raman spectra exhibit the D (1350 cm⁻¹) and G (1590 cm⁻¹) bands expected for graphitic carbon; therefore the carbon capsules are anticipated to possess good electrical conductivity (Fig. S12†). Co@NPCC contains 2.7 wt% nitrogen and 2.8 wt% cobalt by elemental analysis and inductively coupled plasma atomic emission spectroscopy (ICP-AES), respectively.

The N₂ gas sorption isotherms of Co@NPCC were measured at 77 K. The isotherms of this material showed a sharp uptake of N₂ at low relative pressures ($P < 0.1$) and a hysteresis isotherm loop at higher relative pressures ($0.4 < P < 0.95$), indicating the existence of both micro- and mesopores (Fig. 1j). The calculated BET (Brunauer–Emmett–Teller) surface area is 540 m² g⁻¹, while the total pore volume is 0.8 cm³ g⁻¹ at 0.95 bar. The pore size distribution, calculated from the experimental isotherm based on a DFT model, confirms the hierarchical pore structure with the void diameters predominantly distributing around 9 Å, 22 Å, and 33 Å (Fig. S13†). Such textural properties of this material are anticipated to facilitate the accessibility of active sites and promote substrate diffusion during electrocatalytic processes.

ORR activity evaluation

Pt-group materials are the most active and catalytically stable catalysts for the oxygen reduction reaction. However, due to the terrestrial scarcity and high cost, these catalysts are still somewhat limited in practical catalytic applications.¹ One approach to reducing the costs while maintaining activity and stability is the implementation of noble-metal-free catalysts. In this context, the as-prepared Co@NPCC is evaluated as an electrocatalyst for the ORR in alkaline solution. For comparison, here, commercial Pt/C (20% Pt) and Co/NC derived from the direct pyrolysis of ZIF-8CoZn were also measured for comparison purposes. To test Co@NPCC as an ORR catalyst, we first performed cyclic voltammetry (CV) measurements using a conventional three-electrode electrochemical cell in an O₂-saturated aqueous KOH solution at room temperature (Fig. 2a). Compared with the CV curve measured in N₂-saturated 0.1 M KOH, a more prominent cathodic peak at ~0.9 V corresponding to the reduction of O₂ is observed in an O₂-saturated 0.1 M KOH solution (Fig. 2a), highlighting the effective ORR activity of Co@NPCC. Then, the ORR measurements are performed in 0.1 M KOH by using the rotating disk electrode (RDE) technique. The onset potential, half-wave potential and ultimate current densities estimated from these measurements are listed in Table S1†. Co@NPCC shows a more positive onset potential (~1.02 V, *vs.* RHE), half-wave potential (~0.9 V, *vs.* RHE), and higher diffusion-limiting current density (~5.2 mA cm⁻²), which are comparable to those (onset potential ~1.01 V; half-wave potential ~0.91, *vs.* RHE and ~4.8 mA cm⁻²) of commercial Pt/C. Significantly, our obtained results mimic those of the best performing materials reported in the literature (Table S1†). The lower onset and half-wave potentials measured for Co/NC highlight the beneficial impact of generating the hollow nitrogen-doped porous carbon shell, which is easily enabled by our synthetic methodology (Fig. 2b and Table S1†). Additionally, linear sweep voltammograms (LSV) measured at different rotation speeds are obtained to produce the Koutecky–Levich plots of Co@NPCC (Fig. 2c). The fact that these LSVs displayed good linearity and parallelism, under different potentials, establishes that the reaction kinetics toward the dissolved oxygen

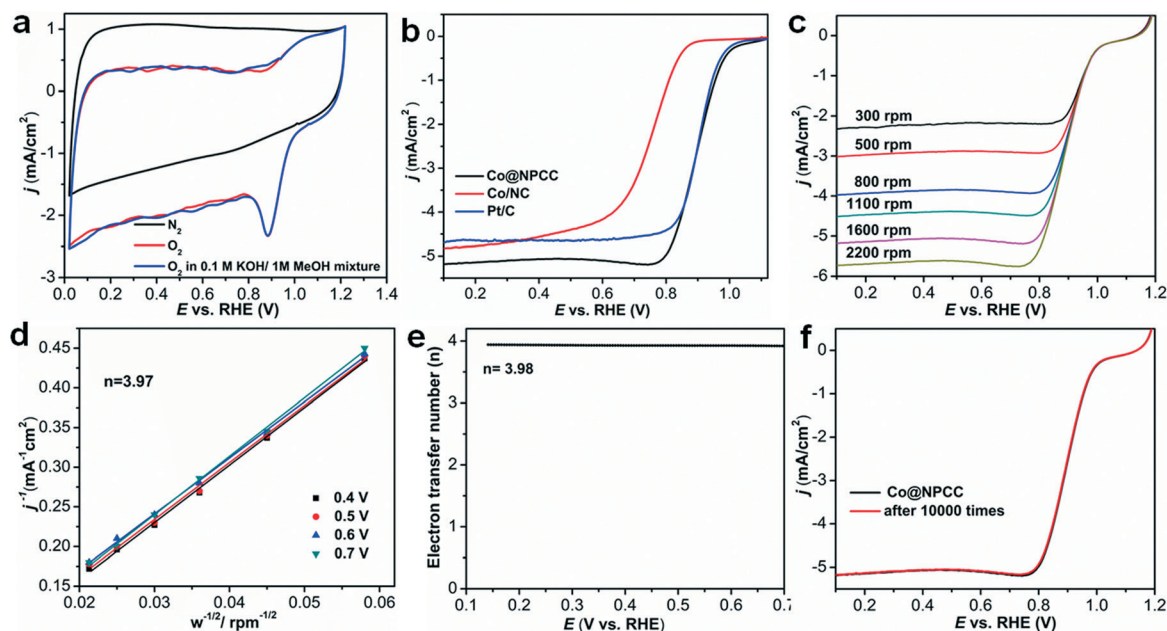


Fig. 2 (a) Cyclic voltammograms of Co@NPCC in N_2 -/or O_2 -saturated 0.1 M KOH, and an O_2 -saturated 0.1 M KOH/1 M MeOH mixture. (b) ORR polarization curves for the various electrocatalysts at a rotation speed of 1600 rpm. (c) LSVs of Co@NPCC under different rotating rates of the disk electrode and (d) the corresponding Koutecky–Levich plots at different potentials. (e) Electron-transfer number of Co@NPCC by the RRDE technique. (f) LSV curves of Co@NPCC before and after 10 000 cycles in an O_2 -saturated 0.1 M KOH solution.

are first-order. The number of electrons transferred was determined in the potential range of 0.4 to 0.7 V and found to be 3.97. This value confirms that a four-electron pathway predominates and that H_2O_2 production is minimal (Fig. 2d). The reaction pathway was further probed using the rotating ring-disk electrode (RRDE) technique. Co@NPCC shows an n value higher than 3.98 in alkaline medium, with HO_2^- formation being lower than 5% over the whole range of potentials, thereby demonstrating its excellent electrocatalytic selectivity (Fig. 2e, S15 and S16[†]). The long-term stability and durability of the Co@NPCC catalyst was retained after accomplishing 10 000 consecutive CV cycles and a chronoamperometric test (Fig. 2f and S17[†]). The TEM and HRTEM images and SAED pattern (Fig. S18[†]) show that the morphology of the Co nanoparticles embedded in the hollow nanostructure is retained after the stability test, indicating a high level of structural stability. Importantly, to examine the fuel crossover effect, Co@NPCC was cycled in an O_2 -saturated 0.1 M KOH/1.0 M methanol mixture. Apparently, there was no distinct change in the current density of Co@NPCC after injecting 1.0 M methanol into the solution (Fig. 2a). This behavior demonstrates that Co@NPCC has excellent tolerance to methanol crossover.

The ORR performance of Co@NPCC was further evaluated in an O_2 -saturated 0.05 M H_2SO_4 solution with the same electrode configuration as that used under alkaline conditions. The polarization curve (RRDE) of Co@NPCC shows that the onset and half-wave potentials are 0.85 V and 0.71 V, respectively (Fig. S19[†]). The RRDE test results revealed that the H_2O_2 yield over Co@NPCC remained below 3% and the number of electrons transferred was determined to be 3.86

(Fig. S20 and S21[†]). These results demonstrated that the catalytic process at the Co@NPCC electrode underwent a four-electron ORR pathway in H_2SO_4 solution. Co/NC showed lower activity.

Taken together, these performance metrics place Co@NPCC in the top tier of oxygen reduction electrocatalysts. The exceptional electrocatalytic activity of this composite can be ascribed to: (i) the electrical conductivity, porosity, and hollow morphology of the nitrogen-doped carbon capsules, which have excellent permeability that facilitates access of the substrates as well as electrons to the catalytic sites; (ii) isolated CoNPs provide a large number of exposed active sites, which are known to improve the electronic interaction between carbon and CoNPs and enhance the electrocatalytic activity; (iii) Co– N_x active sites embedded into the carbon matrix reduce the binding energy for both O_2 adsorption and O=O dissociation.^{55,56}

Conclusions

In summary, this study reported the synthesis and fabrication of hollow nitrogen/cobalt-doped porous carbon capsule supported cobalt nanoparticles (Co@NPCC). The practical application of Co@NPCC has been demonstrated by its use as a highly-efficient electrocatalyst toward the ORR, which significantly surpasses most of the reported non-noble metal catalysts, as well as the commercial Pt/C catalyst. Additionally, the Co@NPCC catalyst at the gram level is easily produced. The strategy presented here to fabricate this catalyst is amenable and scalable. Ultimately, this study is expected to open a new avenue for designing a wide variety of solid

catalysts with tailored morphologies that are of interest for a broad range of applications.

Conflicts of interest

There are no conflicts to declare.

Acknowledgements

This work was supported by the financial support of Yangtze Normal University (011154169) and University of South Florida. The authors extend their appreciation to the Distinguished Scientist Fellowship Program (DSFP) at King Saud University for funding this work partially. V. Bansal acknowledges the Australian Research Council for a Future Fellowship (FT140101285).

Notes and references

- D. Y. Chung, J. M. Yoo and Y. E. Sung, *Adv. Mater.*, 2018, 1704123.
- M. Shao, Q. Chang, J. P. Dodelet and R. Chenitz, *Chem. Rev.*, 2016, 116, 3594–3657.
- M. Li, Z. Zhao, T. Cheng, A. Fortunelli, C. Y. Chen, R. Yu, Q. Zhang, L. Gu, B. V. Merinov, Z. Lin, E. Zhu, T. Yu, Q. Jia, J. Guo, L. Zhang, W. A. Goddard, 3rd, Y. Huang and X. Duan, *Science*, 2016, 354, 1414–1419.
- G. Wu and P. Zelenay, *Acc. Chem. Res.*, 2013, 46, 1878–1889.
- C. Hu and L. Dai, *Angew. Chem., Int. Ed.*, 2016, 55, 11736–11758.
- M. Chen, L. Wang, H. Yang, S. Zhao, H. Xu and G. Wu, *J. Power Sources*, 2018, 375, 277–290.
- W. Xia, A. Mahmood, Z. Liang, R. Zou and S. Guo, *Angew. Chem., Int. Ed.*, 2016, 55, 2650–2676.
- A. A. Gewirth, J. A. Varnell and A. M. DiAscro, *Chem. Rev.*, 2018, 118, 2313–2339.
- C. Zhu, H. Li, S. Fu, D. Du and Y. Lin, *Chem. Soc. Rev.*, 2016, 45, 517–531.
- H. Liu, M. Q. Wang, Z. Y. Chen, H. Chen, M. W. Xu and S. J. Bao, *Dalton Trans.*, 2017, 46, 15646–15650.
- Z. Liu, F. Sun, L. Gu, G. Chen, T. Shang, J. Liu, Z. Le, X. Li, H. B. Wu and Y. Lu, *Adv. Eng. Mater.*, 2017, 7, 1701154.
- Q. Liu and J. Zhang, *Langmuir*, 2013, 29, 3821–3828.
- X. Liu, M. Park, M. G. Kim, S. Gupta, G. Wu and J. Cho, *Angew. Chem., Int. Ed.*, 2015, 54, 9654–9658.
- Y. Liu, H. Jiang, Y. Zhu, X. Yang and C. Li, *J. Mater. Chem. A*, 2016, 4, 1694–1701.
- Y. Su, Y. Zhu, H. Jiang, J. Shen, X. Yang, W. Zou, J. Chen and C. Li, *Nanoscale*, 2014, 6, 15080–15089.
- S. K. Singh, V. Kashyap, N. Manna, S. N. Bhangre, R. Soni, R. Boukherroub, S. Szunerits and S. Kurungot, *ACS Catal.*, 2017, 7, 6700–6710.
- Y. Fu, H.-Y. Yu, C. Jiang, T.-H. Zhang, R. Zhan, X. Li, J.-F. Li, J.-H. Tian and R. Yang, *Adv. Funct. Mater.*, 2018, 28, 1705094.
- Z. Wang, S. Xiao, Z. Zhu, X. Long, X. Zheng, X. Lu and S. Yang, *ACS Appl. Mater. Interfaces*, 2015, 7, 4048–4055.
- F. L. Meng, Z. L. Wang, H. X. Zhong, J. Wang, J. M. Yan and X. B. Zhang, *Adv. Mater.*, 2016, 28, 7948–7955.
- W. Xia, J. Zhu, W. Guo, L. An, D. Xia and R. Zou, *J. Mater. Chem. A*, 2014, 2, 11606–11613.
- J.-S. Li, S.-L. Li, Y.-J. Tang, K. Li, L. Zhou, N. Kong, Y.-Q. Lan, J.-C. Bao and Z.-H. Dai, *Sci. Rep.*, 2014, 4, 5130.
- X. Xu, F. Nosheen and X. Wang, *Chem. Mater.*, 2016, 28, 6313–6320.
- T. Cai, W. Xing, Z. Liu, J. Zeng, Q. Xue, S. Qiao and Z. Yan, *Carbon*, 2015, 86, 235–244.
- G. Wu, A. Santandreu, W. Kellogg, S. Gupta, O. Ogoke, H. Zhang, H.-L. Wang and L. Dai, *Nano Energy*, 2016, 29, 83–110.
- H. Fei, R. Ye, G. Ye, Y. Gong, Z. Peng, X. Fan, E. L. Samuel, P. M. Ajayan and J. M. Tour, *ACS Nano*, 2014, 8, 10837–10843.
- G.-L. Tian, Q. Zhang, B. Zhang, Y.-G. Jin, J.-Q. Huang, D. S. Su and F. Wei, *Adv. Funct. Mater.*, 2014, 24, 5956–5961.
- Z. Yang, Z. Yao, G. Li, G. Fang, H. Nie, Z. Liu, X. Zhou, X. Chen and S. Huang, *ACS Nano*, 2012, 6, 205–211.
- T. V. Vineesh, M. P. Kumar, C. Takahashi, G. Kalita, S. Alwarappan, D. K. Pattanayak and T. N. Narayanan, *Adv. Eng. Mater.*, 2015, 5, 1500658.
- S. Zhao, H. Yin, L. Du, L. He, K. Zhao, L. Chang, G. Yin, H. Zhao, S. Liu and Z. Tang, *ACS Nano*, 2014, 8, 12660–12668.
- Y. Wang, L. Tao, Z. Xiao, R. Chen, Z. Jiang and S. Wang, *Adv. Funct. Mater.*, 2018, 28, 1705356.
- W. Xia, C. Qu, Z. Liang, B. Zhao, S. Dai, B. Qiu, Y. Jiao, Q. Zhang, X. Huang, W. Guo, D. Dang, R. Zou, D. Xia, Q. Xu and M. Liu, *Nano Lett.*, 2017, 17, 2788–2795.
- W. Xia, R. Zou, L. An, D. Xia and S. Guo, *Energy Environ. Sci.*, 2015, 8, 568–576.
- S. You, X. Gong, W. Wang, D. Qi, X. Wang, X. Chen and N. Ren, *Adv. Eng. Mater.*, 2016, 6, 1501497.
- Q. L. Zhu, W. Xia, T. Akita, R. Zou and Q. Xu, *Adv. Mater.*, 2016, 28, 6391–6398.
- L. Shang, H. Yu, X. Huang, T. Bian, R. Shi, Y. Zhao, G. I. Waterhouse, L. Z. Wu, C. H. Tung and T. Zhang, *Adv. Mater.*, 2016, 28, 1668–1674.
- B. Y. Guan, X. Y. Yu, H. B. Wu and X. W. D. Lou, *Adv. Mater.*, 2017, 29, 1703614.
- Y.-Z. Chen, R. Zhang, L. Jiao and H.-L. Jiang, *Coord. Chem. Rev.*, 2018, 362, 1–23.
- K. Shen, X. Chen, J. Chen and Y. Li, *ACS Catal.*, 2016, 6, 5887–5903.
- Y. Z. Chen, C. Wang, Z. Y. Wu, Y. Xiong, Q. Xu, S. H. Yu and H. L. Jiang, *Adv. Mater.*, 2015, 27, 5010–5016.
- S. Ma, G. A. Goenaga, A. V. Call and D. J. Liu, *Chem. – Eur. J.*, 2011, 17, 2063–2067.
- W. Chaikittisilp, N. L. Torad, C. Li, M. Imura, N. Suzuki, S. Ishihara, K. Ariga and Y. Yamauchi, *Chem. – Eur. J.*, 2014, 20, 4217–4221.
- A. Aijaz, J. Masa, C. Rosler, W. Xia, P. Weide, A. J. Botz, R. A. Fischer, W. Schuhmann and M. Muhler, *Angew. Chem., Int. Ed.*, 2016, 55, 4087–4091.

- 43 Z. Li, M. Shao, L. Zhou, R. Zhang, C. Zhang, M. Wei, D. G. Evans and X. Duan, *Adv. Mater.*, 2016, **28**, 2337–2344.
- 44 J. Meng, C. Niu, L. Xu, J. Li, X. Liu, X. Wang, Y. Wu, X. Xu, W. Chen, Q. Li, Z. Zhu, D. Zhao and L. Mai, *J. Am. Chem. Soc.*, 2017, **139**, 8212–8221.
- 45 H. Zhang, H. Osgood, X. Xie, Y. Shao and G. Wu, *Nano Energy*, 2017, **31**, 331–350.
- 46 Y. Li, B. Jia, Y. Fan, K. Zhu, G. Li and C.-Y. Su, *Adv. Eng. Mater.*, 2018, **8**, 1702048.
- 47 S. Bhattacharyya, B. Konkena, K. Jayaramulu, W. Schuhmann and T. K. Maji, *J. Mater. Chem. A*, 2017, **5**, 13573–13580.
- 48 S. Gadipelli, T. Zhao, S. A. Shevlin and Z. Guo, *Energy Environ. Sci.*, 2016, **9**, 1661–1667.
- 49 Q. Ren, H. Wang, X. F. Lu, Y. X. Tong and G. R. Li, *Adv. Sci.*, 2018, **5**, 1700515.
- 50 Y. V. Kaneti, J. Tang, R. R. Salunkhe, X. Jiang, A. Yu, K. C. Wu and Y. Yamauchi, *Adv. Mater.*, 2017, **29**, 1604898.
- 51 P. Yin, T. Yao, Y. Wu, L. Zheng, Y. Lin, W. Liu, H. Ju, J. Zhu, X. Hong, Z. Deng, G. Zhou, S. Wei and Y. Li, *Angew. Chem., Int. Ed.*, 2016, **55**, 10800–10805.
- 52 Q.-L. Zhu, W. Xia, L.-R. Zheng, R. Zou, Z. Liu and Q. Xu, *ACS Energy Lett.*, 2017, **2**, 504–511.
- 53 D. Zhao, J. L. Shui, L. R. Grabstanowicz, C. Chen, S. M. Commet, T. Xu, J. Lu and D. J. Liu, *Adv. Mater.*, 2014, **26**, 1093–1097.
- 54 H. Yang, S. J. Bradley, A. Chan, G. I. N. Waterhouse, T. Nann, P. E. Kruger and S. G. Telfer, *J. Am. Chem. Soc.*, 2016, **138**, 11872–11881.
- 55 T. S. Olson, S. Pylypenko, P. Atanassov, K. Asazawa, K. Yamada and H. Tanaka, *J. Phys. Chem. C*, 2010, **114**, 5049–5059.
- 56 S.-T. Chang, C.-H. Wang, H.-Y. Du, H.-C. Hsu, C.-M. Kang, C.-C. Chen, J. C. S. Wu, S.-C. Yen, W.-F. Huang, L.-C. Chen, M. C. Lin and K.-H. Chen, *Energy Environ. Sci.*, 2012, **5**, 5305–5314.